Journal of Solid State Chemistry 183 (2010) 2389–2399

Contents lists available at ScienceDirect

Journal of Solid State Chemistry

journal homepage: www.elsevier.com/locate/jssc

Role of surface hydroxyl groups in promoting room temperature CO sensing by Pd-modified nanocrystalline SnO_2

Artem V. Marikutsa, Marina N. Rumyantseva, Lada V. Yashina, Alexander M. Gaskov *

Chemistry Department, Moscow State University, Moscow 119991, Russia

ARTICLE INFO

Article history:
Received 17 March 2010
Received in revised form
15 June 2010
Accepted 10 July 2010
Available online 17 July 2010

Keywords:
Nanocrystalline tin dioxide
Surface hydroxyl groups
Surface modifying
Room temperature sensitivity
Humidity
Palladium

ABSTRACT

SnO_2/Pd nanocomposites were synthesized via sol–gel method followed by variable processing procedures. The materials are sensitive to CO gas in the concentration range 2–100 ppm at room operating temperature. It was shown that modification of nanocrystalline tin dioxide by Pd changes the temperature dependence of sensor response, decreasing the temperature of maximal signal. To understand the mechanism of room temperature CO sensitivity, a number of SnO_2/Pd materials were characterized by XRD, TEM, BET, XPS and TPR techniques. From the results of FTIR, impedance and sensing measurements under variable ambient conditions it was concluded that improvement in CO sensitivity for Pd-modified SnO_2 is due to alteration of CO oxidation pathway. The reaction of CO with surface OH-groups at room temperature was proposed, the latter being more reactive than oxygen species due to the possible chain character of the reactions. It was proposed that Pd additive may initiate chain processes at room temperature.

1. Introduction

Semiconductor tin dioxide based gas sensing materials have been attracting a great interest due to their high sensitivity to harmful gases at ppm concentration level and the compactness of sensing devices. Atomic defects in SnO_2 structure are singly and doubly charged oxygen vacancies determining *n*-type semiconductor properties [1], the electron concentration and electric conductivity of the material being strongly dependent on the ambient gas composition. The main pathways of sensor signal formation are as follows: (a) chemisorption on the crystallite surface with the formation of surface acceptor- or donor-like electronic states and (b) surface reaction of the chemisorbed species with gas molecules. The material grain size is an important parameter influencing gas sensitivity. According to Korotcenkov et al. [2] response to CO increases significantly when lowering particle size of SnO_2 from 100 to 2 nm. Such an increase is reported to be slow for grain size larger than double depletion layer thickness ($2L_d$) and dramatic for particles less than $2L_d$ [3]. Baraton et al. [4] have shown that SnO_2 with grain size less than 8–10 nm possesses improved CO sensitivity compared with less dispersive samples due to the larger specific surface area available for chemisorption and surface reaction processes.

CO gas detection is an important task of personal safety, especially in the regions of motor transport congestion. An encouraging problem is incorporating CO sensors into mobile phones or other autonomic devices. However, CO can be reliably detected only at relatively high temperatures that are unacceptable for wireless detectors due to high power consumption and low stability of the sensing material. Hence there is the need for room temperature (RT) CO sensors. It has been shown that a response to CO develops via oxidation of CO molecules by chemisorbed oxygen species O^- or O_2^- with the formation of CO_2 and chemisorbed CO_3^- species (as indicated in the FTIR experiments) [5]. Such reactions are known to proceed at temperatures as high as 250–350 °C only [6]. Recently, a number of works concerned with CO detection at low or room temperature have been reported, almost each of them dealing with tin dioxide or ITO, modified by noble metal additives. Among the studied composites are Au–SnO_2 [7,8], Pt–ITO and Au–ITO [9], Pt–SnO_2 [10–12], Pt–Pd–SnO_2 [13], Ag_2O–SnO_2 [10], PdO–CuO–SnO_2 [14], PdO–CeO_2–SnO_2 [15], etc.

The most common approach to improving sensor response and selectivity towards CO is doping of tin dioxide with Pd [16–20]. The SnO_2/Pd system has been extensively studied; most of the obtained data on the sensibilization effect of Pd towards CO refer to the high temperature sensors behavior. There are several explanations of the sensibilization effects upon introduction of the Pd additives, e.g. CO spill-over on the PdO grain boundaries [17], direct CO oxidation by PdO attached to the SnO_2 surface [1,14,17], modulation of intragrain electric properties by Pd^{2+} incorporation into the SnO_2 lattice [16], etc. Recently it has been shown that the surface hydroxyl groups of the nanocrystalline

* Corresponding author. Fax: +7 495 9390998.
E-mail addresses: artem.marikutsa@gmail.com (A.V. Marikutsa), roum@inorg.chem.msu.ru (M.N. Rumyantseva), yashina@inorg.chem.msu.ru (L.V. Yashina), gaskov@inorg.chem.msu.ru (A.M. Gaskov).

0022-4596/$ - see front matter © 2010 Elsevier Inc. All rights reserved.
doi:10.1016/j.jssc.2010.07.017

SnO_2/Pd play an important role in detecting CO that should not be underrated [21,22,19]. Hydroxyl groups chemisorption onto the surface of tin dioxide based sensors is inevitable, since the latter are usually used in humid ambient air. Gerher and Cox [23] have shown that 10–15% of adsorbed water on the surface of a SnO_2 single crystal undergoes dissociation at Lewis acidic and basic centers yielding OH groups bound to the cations (isolated hydroxyls) and the protons bound to lattice O^{2-} ions (“rooted” hydroxyls), respectively. Although the possibility of hydroxyls reaction with CO on the surface of pure SnO_2 was suggested earlier [17], Barsan and co-workers [21,19] observed a significant activation of OH groups with regard to the CO oxidation when tin dioxide was doped with Pd; however the role of Pd was unclear. Nevertheless, the electric measurements were performed at temperatures 250–300 °C and DRIFT spectra of SnO_2/Pd recorded at RT were interfered by an alumina substrate [22].

In this work we report on the synthesis of nanocrystalline SnO_2 materials modified by Pd and the investigation of their sensitivity to CO gas under variable conditions. The main objective of the present work is to understand the mechanism of the sensibilization effect of Pd, resulting in sensitivity to CO at room temperature. Application of different techniques (FTIR, impedance and XPS) under variable conditions allowed us to conjecture the processes of CO interaction with the surface species on SnO_2/Pd surface at low temperatures.

2. Materials and methods

2.1. Preparation of nanocrystalline SnO_2 and its modification with Pd

Nanocrystalline SnO_2 was synthesized via a precipitation route: 0.1 M aqueous solution of NH_4OH was slowly added to stirred solution of 0.3 M $SnCl_4 \cdot 5\,H_2O$ in deionized water until pH 6 was reached, according to the following reaction:

$$SnCl_4 + 4NH_3 \cdot H_2O + (n-2)H_2O = SnO_2 \cdot nH_2O \downarrow + 4NH_4Cl. \quad (1)$$

The formed precipitate was centrifuged, washed several times with deionized water to remove Cl^- ions (the residual chloride was tested with 0.05 M aqueous solution of $AgNO_3$) and dried at 50 °C overnight. The obtained $SnO_2 \cdot nH_2O$ powder was divided into three parts. Two of them were annealed at 300 and 500 °C, respectively, for 24 h to produce samples of nanocrystalline SnO_2 with various crystallite sizes. The third part of $SnO_2 \cdot nH_2O$ powder was used for the synthesis of Pd-doped SnO_2 samples.

The modifying of SnO_2 by Pd was carried out via an impregnation method. The nominal quantity of modifier was 1 wt% of Pd in SnO_2/Pd nanocomposites. 1.2 g of dried $SnO_2 \cdot nH_2O$ powder was dispersed in 20 ml ethanol solution of $Pd(acac)_2$ and evaporated upon heating and stirring. The impregnated SnO_2–$Pd(acac)_2$ subproduct was calcined at 250, 300 or 500 °C for 24 h. The temperature 250 °C was used as the lowest temperature of $Pd(acac)_2$ decomposition that was proven by TG-DSC. To study the treatment effect, two samples of SnO_2/Pd series were synthesized via impregnation of $Pd(acac)_2$ into SnO_2-300 powder. The obtained SnO_2-300–$Pd(acac)_2$ subproduct was annealed at 250 °C or at 300 °C for 24 h. The respective sample designations and conditions of their synthesis are compared in Table 1.

2.2. Materials characterization

Phase composition and crystal structure were determined by X-ray diffraction measurements. The crystallite size (d_{XRD}) of SnO_2 was calculated from the broadening of the (110) XRD peak using the Scherer equation, with wavelength $\lambda = 1.54051$ Å (Cu$K\alpha$ radiation). The microstructure of SnO_2/Pd samples was characterized by transmission electron microscopy (TEM) (LEO 912 AB OMEGA). The specific surface area of powders was measured by the BET method of nitrogen adsorption using a Chemisorb 2750 instrument from Micromeritics.

The XPS spectra were collected using an Axis Ultra DLD (Kratos, UK) spectrometer equipped with a monochromatic Al$K\alpha$ X-ray source (analysis area $300 \times 700\ \mu m^2$). The spectra were recorded at constant analyzer pass energy (*PE*) of 5 eV (yielding resolution better than 0.4 eV) and *PE* = 80 eV (to ensure high elemental sensitivity). The energy scale was calibrated using the following peak positions: Au $4f_{7/2}$ – 83.96 eV, Cu $2p_{3/2}$ – 932.62 eV, Ag $3d_{5/2}$ – 368.21 eV, Pd $3d_{5/2}$ – 338.08 eV with the accuracy better than × 0.05 eV. In the case of SnO_2 samples charge neutralization was applied, providing the C 1*s* peak position of 285.0 eV. The analyzer transmission function was also calibrated. All spectra were collected at normal emission. For the data analysis, the XP-spectra were fitted by the Gaussian–Lorentzian convolution functions with simultaneous optimization of the background parameters. To study the effect of ambient gas on the elements oxidation state, the XPS spectra were collected for samples exposed *ex situ* to 100 ppm CO in air (25 °C). After spectra acquisition the samples were exposed to air for several hours and then measured again.

Characterization of surface species of the samples was carried out by means of Temperature Programmed Reduction by H_2 (TPR-H_2) using the Chemisorb 2750 (Micromeritics) instrument. The powders were tested without any pre-treatment.

2.3. Conductance, impedance and FTIR measurements under variable ambient conditions

To perform sensing tests, thick films of nanocrystalline gas-sensitive powders were screen-printed onto alumina substrates. Vapor-deposited gold contacts with pressed platinum wires were fitted to the substrate. A platinum heater was attached to the back side of the substrate. The conductance measurements were

Table 1
Sample designations, synthesis conditions, phase composition and microstructure characterization.

Sample designation	T_{anneal} (SnO_2) (°C)	Additive	T_{anneal} (impregnated SnO_2) (°C)	Phase composition (d_{XRD}, nm)[a]	BET surface (m^2/g)
SnO_2-300	300	–	–	SnO_2 (3–4)	95
SnO_2-500	500	–	–	SnO_2 (10–12)	35
SnO_2–Pd-250	–	$Pd(acac)_2$	250	SnO_2 (2–3)	120
SnO_2–Pd-300	–	$Pd(acac)_2$	300	SnO_2 (2–4)	100
SnO_2-300–Pd-300	SnO_2-300	$Pd(acac)_2$	250	SnO_2 (3–5)	95
SnO_2-300–Pd-300	SnO_2-300	$Pd(acac)_2$	300	SnO_2 (3–5)	90
SnO_2–Pd-500	–	$Pd(acac)_2$	500	SnO_2 (8–11)	40

[a] Calculated from SnO_2 (110) peak broadening using Scherer equation.

performed in a D.C. mode at a constant voltage of 3 V. The experiments were conducted *in situ* under atmosphere changing from pure air (background gas) to a mixture of CO with air (test gas) and vise versa. The sensor signal–temperature dependencies were recorded in the temperature range of 25–300 °C using 100 ppm CO in air as the test gas; the measurements were performed at variable relative humidity (5%, 15% and 30% r.h.). The sensor signal-CO concentration dependencies were recorded at 25 °C under 15% r.h.; the test gas was 2–100 ppm CO in air. The sensor signal was calculated from the following equation:

$$S = R_{air}/R_{CO}, \quad (2)$$

where R_{air} is sensor resistance under the background gas and R_{CO} is resistance under the test gas.

The impedance spectra were recorded using the Impedancemeter Z-3000X (Elins) instrument in the frequency range 3 MHz–10 Hz. Fitting procedure was made in the Z-View 2.3 software; fit errors did not exceed 5% of the calculated value. The sample powders were pressed into pellets. To evaluate the contributions of electronic and protonic conductance into the whole impedance the Hebb–Wagner polarization method was used. Protons blocking gold contacts were vapor-deposited onto the pellets. The protonic contribution was obtained by subtracting stationary D.C. electronic conductance (after polarization achievement) from the mixed conductance measured in A.C. mode. The impedance measurements were performed *in situ* at room temperature under the atmosphere changing from air of 20% r.h. through air of 5% r.h. to the mixture of 100 ppm CO with air at 5% r.h.

FTIR transmission spectra were recorded using a Spectrum One (Perkin Elmer) spectrometer in the wave number region of 4000–370 cm^{-1}. The samples (2.0 mg of powder) were pressed into pellets with 100.0 mg KBr. The measurements were performed at room temperature under air (20% r.h.) and after preliminary annealing at 250 °C and cooling down to room temperature under air (4% r.h.), in order to examine the humidity influence on the surface species composition.

3. Results and discussion

3.1. Composition and microstructure of samples

The X-ray diffraction patterns of the pristine and Pd-loaded tin dioxide powders are reported in Supplementary Data (Figure XRD). The phase evaluation and average particle size (d_{XRD}) calculated using the Scherer formula are summed up in Table 1. The samples annealed at or below 300 °C consist of the nanocrystalline cassiterite phase, with tin dioxide particle size ranging from 2 to 5 nm for different powders. The dried $SnO_2 \cdot nH_2O$ powder could be either cassiterite particles with a size of 1–2 nm or an amorphous phase with uniformly distributed crystalline nuclei. The samples SnO_2-500 and SnO_2–Pd-500 consist of the cassiterite phase with the average SnO_2 crystallite size of 8–12 nm. The d_{XRD} values of SnO_2 in various samples correlate with the samples' annealing temperatures, and Pd doping has no significant effect on the tin dioxide particle size. No phases corresponding to Pd additive were detected in the SnO_2/Pd samples. This could have been due to either the small modifier content or segregation of Pd derivatives on the tin dioxide grain boundaries. It has been reported that Pd tends to form small clusters of PdO attached to the SnO_2 crystallites surface in Pd-doped tin dioxide nanocomposites prepared by a wet chemical route similar to that used in this work [18].

The BET specific surface areas of the samples are compared in Table 1. The ultradispersive samples annealed at or below 300 °C displayed a fairly large surface area of ≥ 100 m^2/g, in contrast to rougher SnO_2-500 and SnO_2–Pd-500 powders annealed at 500 °C, which had the BET area of 40 m^2/g. The modifying of tin dioxide by Pd had a minor effect on the surface area.

TEM investigation of ultradispersive SnO_2/Pd powders enabled the visualization of agglomerated tin dioxide particles only. A micrograph of the sample SnO_2-300–Pd-300 is presented in Fig. 1, the micrographs of other ultradispersive samples all being similar to this one. Most of the particles have a spherical shape and a size ranging from 2 to 6 nm, which is in accordance with the calculations of d_{XRD} from the XRD data. Electron diffraction (ED) (see Supplementary Data, Table ED) confirmed the presence of cassiterite phase in the SnO_2/Pd samples. Particles or clusters of palladium containing phases were not distinctly observed by TEM, nor were they detected by ED. This may be explained by the fact that the atomic numbers of palladium and tin are close (46 and 50, respectively), which leads to similar electron sputtering behavior of the elements, so that distinguishing Pd-containing phase on the SnO_2 background by contrast is rather difficult, if possible.

However, the palladium band was detected by means of XPS analysis. The XP-spectrum of Pd element in the SnO_2/Pd samples is shown in Fig. 2 and those of Sn and O elements in Fig. 3. The Pd 3*d* spectrum may be fitted with two doublets and low intensive band shifted to higher binding energy (BE). The assignment of the observed peaks to Pd states is a somewhat ambiguous procedure. Here we suggest the most probable explanation from our point of view. Regarding the doublets, the minor peak positioned at 335.9 eV could be assigned to the elemental Pd^0 state, with the shift of 0.8 eV relative to the bulk metallic Pd (335.08 eV). Such a shift may be due to a number of factors: (a) metal–support interaction, known for Pd–Al_2O_3 [24], Pd–Beta Zeolite catalysts [25]; (b) nanosize-induced BE shift [24,26,27], this shift being due to quantum confinement effects, changes in metal–metal coordination and bond lengths [26]; (c) changes in local coordination of side ligands [28]; (d) final state effects related to core–hole shielding, slow charge relaxation in metals deposited on insulating supports [29]. For Pd-clusters deposited on SnO_2 the Pd $3d_{5/2}$ peak shift to higher BE may be attributed to nanosize

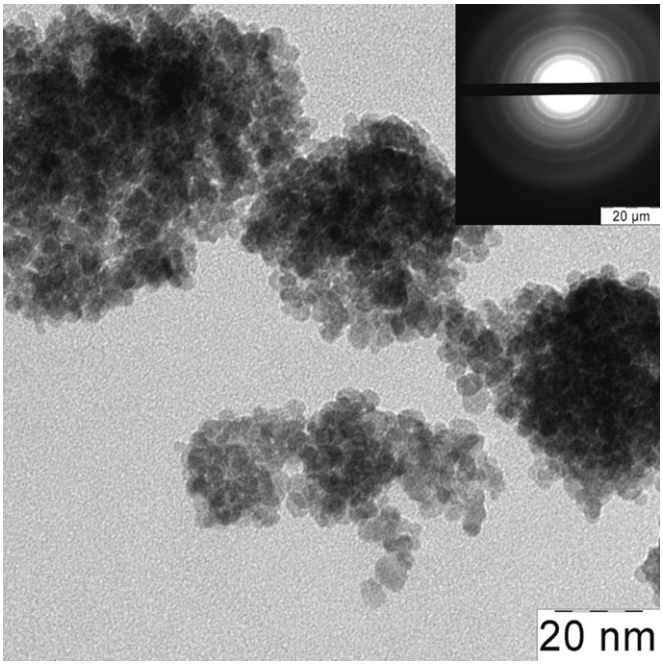

Fig. 1. TEM micrograph and electron diffraction picture (in the inset) of the SnO_2-300–Pd-300 sample. Other nanocrystalline SnO_2/Pd samples displayed similar results.

effect, according to Chichova et al. [27], where the shift in the range 335.4–336.3 eV was ascribed to Pd cluster size decrease with no regard to metal–support interaction. Furthermore, SnO_2 is not an insulating support, so slow charge relaxation (final state effect) might be also neglected. According to literature data the position of Pd^0 peak 335.9 eV can correspond to Pd clusters with size slightly larger than 1.5–2 nm (336.1 eV [24]) but less than 5.5 nm (335.2 eV [26]). Another evidence of Pd^0 clusters formation in the SnO_2/Pd samples is a low intensive band at BE ~ 347 eV, which can be attributed to plasmon losses band [24]. The presence of unoxidized Pd could be due to its epitaxial contact with the SnO_2 surface [1].

The predominant doublet contributing to Pd $3d_{5/2}$ XP-spectrum shown in Fig. 2 is centered at 337.7 eV and indicates an oxidized form of Pd additive. Taking into account the nanosize shift of Pd^0 clusters, we suppose that such is the case for the other form of Pd. This peak is ascribed to Pd^{2+} state, which is quite in agreement with the literature data [28,29]. This palladium state can be attributed to PdO, with BE upshifted due to nanosize effect, local Pd^{2+} coordination disturbance compared to pure PdO as a result of small coordination number or impurities (e.g. Cl^-) coordination [28].

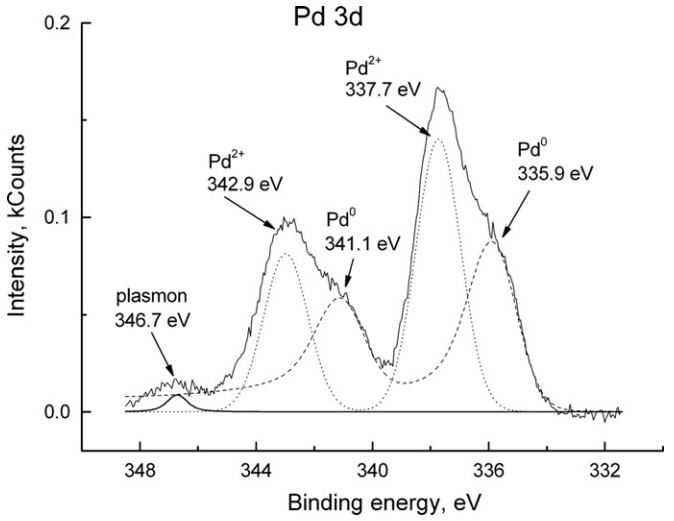

Fig. 2. XPS spectrum Pd element in the nanocrystalline SnO_2/Pd samples, room conditions (air 20% r.h., T=25 °C). Pass energy: 80 eV.

Based on the above-mentioned data, we believe that the SnO_2/Pd powders represent tin dioxide nanocrystals covered with Pd clusters (i.e. PdO/Pd) attached to the grain boundaries of SnO_2. Moreover, island (non-continuous) way of Pd growth on SnO_2 surface has been stated in [27]. The Pd concentration in the SnO_2/Pd nanocomposites was calculated from the XPS data as 0.3 at% (which equals to 0.6 wt% of Pd). This result is in good agreement with Pd concentration evaluated by laser-ionization mass-spectrometry (0.3–0.4 at% for all the nanocomposites). The difference between practical (0.6 wt%) and nominal Pd concentrations (1 wt%) can be attributed to partial $Pd(acac)_2$ evaporation during samples processing procedure.

The XP-spectrum of the O 1*s* region (Fig. 3) consists of an asymmetrical peak that may be fitted with at least two regular peaks. One of them, centered at 530.5 eV, supposedly corresponds to the lattice O^{2-} ions, while the second peak shifted towards higher binding energy (531.6 eV) might be due to the strongly bound surface species such as O^-, O_2^- or hydroxyls. The less bonded species were lost by surface under UHV conditions. The relative concentration of oxygen in these two forms was found to vary during the measurements probably due to X-ray promoted desorption or decomposition of strongly bound surface species. The position of Sn $3d_{5/2}$ peak (486.7 eV) indicates that tin atoms are tetravalent, thus corresponding to the SnO_2 phase.

The presence of surface species in the ultradispersive SnO_2-300 and SnO_2/Pd samples, deduced from the existence of higher binding energy component of O 1*s* peak in the XP-spectra, was further confirmed in the TPR-H_2 experiment. The TPR spectra of nanocrystalline SnO_2 and SnO_2/Pd samples (Fig. 4) illustrate the rate of H_2 consumption as a function of temperature. We attribute the strong peaks in the region of 400–570 °C to the reduction of bulk SnO_2:

$$SnO_{2(s)} + 2H_{2(g)} = Sn_{(s)} + 2H_2O_{(g)}. \quad (3)$$

This assignment can be confirmend by the fact that at the end of the experiments the samples were completely reduced to metallic state and looked like small metallic (tin) drops. The weaker peaks at 100–300 °C in the TPR spectra of ultradispersive samples (Fig. 4a) seem to result from the reduction of the surface species, such as hydroxyls or chemisorbed oxygen derivatives that may be schematically described by the following processes:

$$O^-_{(surf)} + H_{2(g)} = H_2O_{(g)} + e^-, \quad (4)$$

$$OH_{(surf)} + H_{2(g)} = 2H_2O_{(g)}. \quad (5)$$

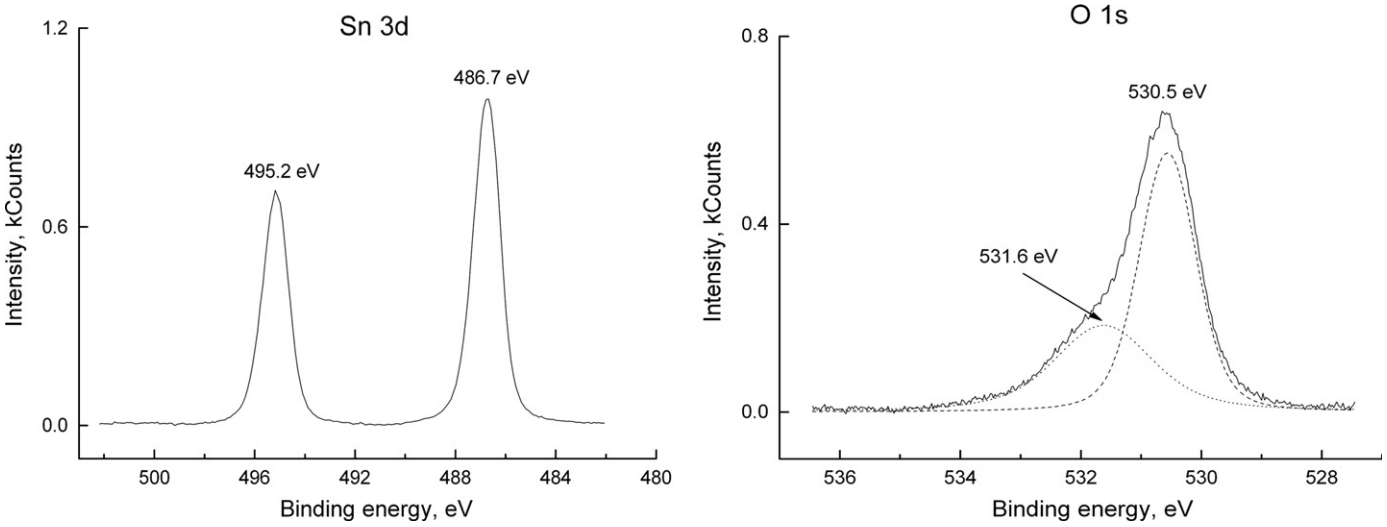

Fig. 3. XPS spectrum of Sn and O elements in the nanocrystalline SnO_2/Pd samples, room conditions (air 20% r.h., T=25 °C). Pass energy: 5 eV.

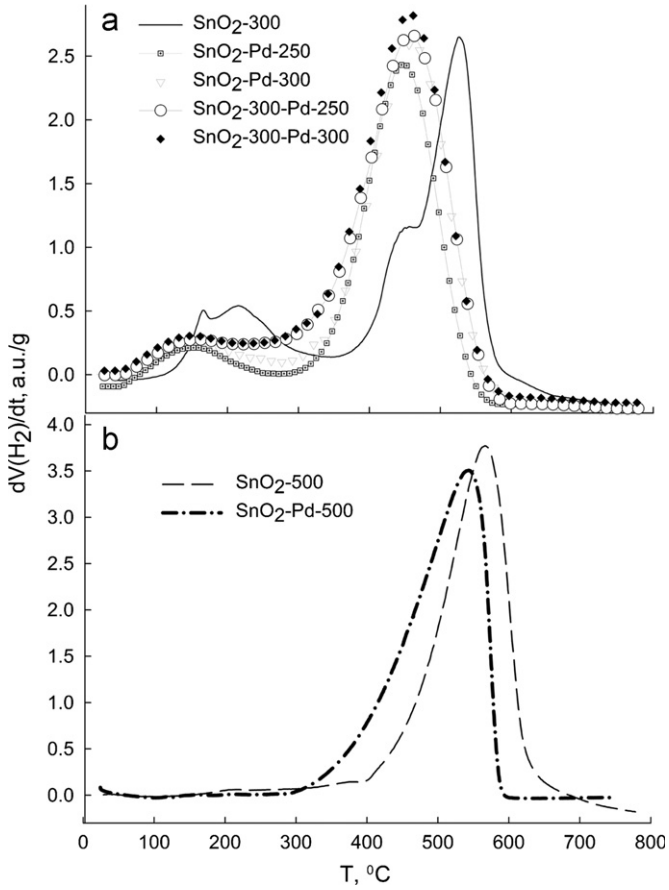

Fig. 4. TPR spectra of ultradispersive (a) and rougher (b) SnO_2 and SnO_2/Pd samples.

Table 2
Evaluation of surface species concentration on the ultradispersive SnO_2 and SnO_2/Pd samples.

Sample	$[O^-]_{surf}$[a], 10^{-5} mol/m^2
SnO_2-300	2.7
SnO_2–Pd-250	1.9
SnO_2–Pd-300	2.4
SnO_2-300–Pd-300	3.6
SnO_2-300–Pd-300	3.6

[a] Calculated for the surface species settled to be O^-.

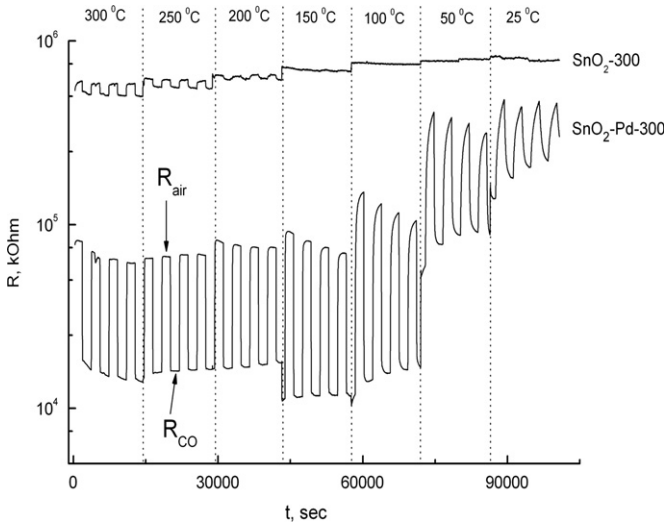

Fig. 5. Resistance of SnO_2- and SnO_2/Pd-based sensors as a function of ambient gas composition (pure air or 100 ppm CO in air) and temperature, 15% r.h.

This assumption is supported by the fact that the SnO_2-500 and SnO_2–Pd-500 samples with smaller BET area displayed no considerable hydrogen consumption in the low temperature region (Fig. 4b), which may be due to the significantly lower concentration of the surface species on the less dispersive powders.

Of particular interest is the shift of TPR peaks for surface species towards lower temperature when tin dioxide is modified by PdO/Pd (Fig. 4a): the peak for SnO_2-300 sample is centered at 230 °C, while those for SnO_2/Pd are centered at 140 °C. This shift may indicate that the surface species of ultradispersive SnO_2/Pd samples are more reactive with regard to hydrogen oxidation than the surface species of undoped SnO_2. On the other hand the downwards peak shift could be due to the catalytic action of the reduced Pd additive. Calculation of the area under TPR curves in 100–300 °C region allows evaluating the surface species concentration. For this purpose an assumption should be made about the predominant TPR reaction to establish a stoichiometric relation between the amounts of the consumed H_2 and the reduced surface species. Here we consider a surface layer consisting of O^- species only, so that the TPR process at 100–300 °C is supposed to be the reaction (4); the calculation results are compared in Table 2. It is clear that the impact of SnO_2 modifying by PdO/Pd on the surface species concentration depends on the synthesis procedure. The samples SnO_2–Pd-250 and SnO_2–Pd-300 obtained through impregnation of dried $SnO_2 \cdot nH_2O$ powder exhibit smaller or close concentrations in comparison to the undoped sample. On the contrary, modifying of calcined SnO_2-300 powder by PdO/Pd leads to an increase of the surface species concentration. It can hardly be due to the difference in the Pd concentration, for the latter was found by XPS to amount to 0.3 at%. Hence, the results of the TPR measurements may be attributed to the influence of the modifying procedure on the concentration of such adsorbates as O^-, O_2^-, hydroxyls, etc. Unfortunately, the TPR method does not allow distinguishing between them and represents a summary effect only.

3.2. CO sensitivity under variable temperature, Humidity and CO concentration

Fig. 5 represents a typical resistance plot of nanocrystalline SnO_2- and SnO_2/Pd-based sensors under an *in situ* changed atmosphere from pure air (5% r.h.) to 100 ppm CO in air (5% r.h.) and vise versa at a variable operating temperature. The CO sensor signal was determined as a ratio of resistance under air to that in the presence of CO (see Eq. (2)); the obtained response values for various samples as a function of temperature are shown in Fig. 6. The results obtained at elevating temperature mode (from 25 to 300 °C) coincide with those obtained at lowering temperature mode (from 300 to 25 °C). From Fig. 6 it may be concluded that modifying SnO_2 samples by PdO/Pd results in the increase of the CO response for all of the studied SnO_2/Pd samples. However, the ultradispersive SnO_2/Pd samples demonstrated the most interesting behavior. Firstly, they displayed a fairly high and reversible CO response even at room temperature and, secondly, had an altered sensor signal–temperature dependence compared with the ultradispersive SnO_2-300 and rougher SnO_2-500 and SnO_2–Pd-500 materials. The responses of the latter increased with temperature in the whole studied region of 25–300 °C, while the ultradispersive SnO_2/Pd sensors displayed maximum CO

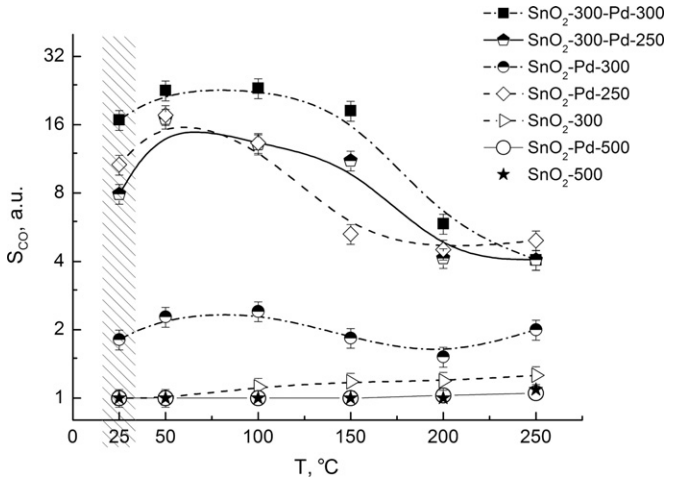

Fig. 6. Sensor signal (S_{CO}) – temperature dependence for SnO_2- and SnO_2/Pd-based sensors, 15% r.h.

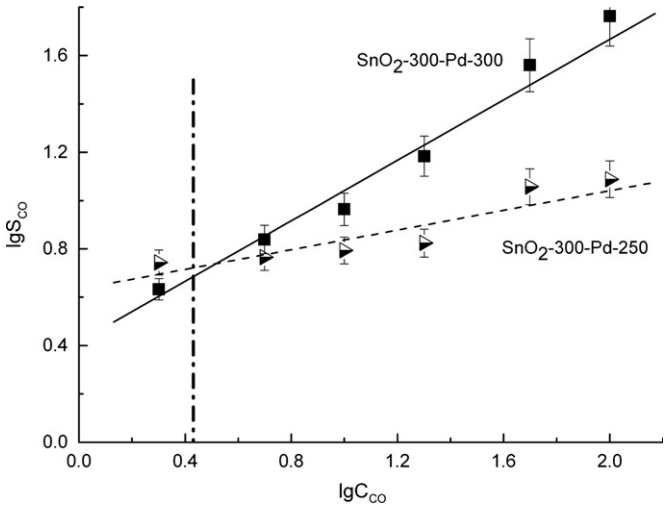

Fig. 7. Sensor signal – CO concentration dependence in logarithmic ordinates for some SnO_2/Pd-based sensors, T=25 °C, 15% r.h. Vertical dash-dot line shows ambient air standard of CO on the lgC_{CO} axis.

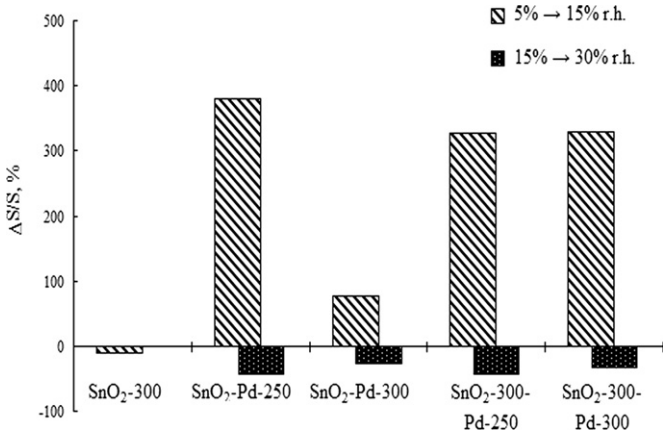

Fig. 8. Relative CO response change for the ultradispersive SnO_2- and SnO_2/Pd-based sensors induced by relative humidity rise at 100 °C.

sensitivity at 50–100 °C. The explanation of these phenomena could lie in the PdO/Pd particles growth and/or agglomeration at elevated annealing temperatures. Moreover, the temperatures of 250 and 300 °C are rather close to the $Pd(acac)_2$ decomposition temperature; thus this may promote the formation of small PdO/Pd clusters. These clusters attached to the tin dioxide surface are likely to contribute to the CO oxidation on the surface of nanocomposites and possibly change it, which is supported by the alteration of the response–temperature dependence.

The effect of nanocomposites treatment was that the SnO_2-300–Pd-300 sample exhibited the highest CO sensitivity (Fig. 6) in the whole temperature range studied in the experiments (response to 100 ppm CO at RT about 16 a.u.). The SnO_2-300–Pd-250 and SnO_2–Pd-250 sensors had mutually similar sensitivity, while the lowest responses were observed for the SnO_2–Pd-300 sample. However, all the ultradispersive SnO_2/Pd materials had similar response–temperature dependences. Hence the difference in the sensor properties of these materials is rather quantitative than qualitative. It is supposed that modifying of calcined SnO_2-300 rather than dried $SnO_2 \cdot nH_2O$ powder yields more CO sensitive material. In the former case the direct PdO/Pd clusters formation can take place on the SnO_2 grain boundaries, while in the latter case the simultaneous emission of $Pd(acac)_2$ decomposition products and water from $SnO_2 \cdot nH_2O$ may prevent PdO/Pd segregation on the SnO_2 surface. The higher CO response of SnO_2-300–Pd-250 and SnO_2-300–Pd-300 could also be anticipated from the TPR data, since these were found to exhibit higher surface species concentration than other samples. The observed similarity of the SnO_2-300–Pd-300 and SnO_2–Pd-250 sensors sensitivities may be due to the higher BET area of the latter.

Fig. 7 illustrates the sensor signal–CO concentration dependence for the SnO_2-300–Pd-300 and SnO_2-300–Pd-300 sensors. These nanocomposites exhibit responses as much as 5.5 and 4.3, respectively, to 2 ppm CO that is below the ambient air standard of CO (2.7 ppm) at room temperature. This is of particular interest in view of the practical application of the room temperature CO sensors. Since the plots are well fitted by straight lines in the logarithmic ordinates, the dependence can be referred to a general power relation, which is common for any sensing material and tested gas:

$$S \sim C_{CO}^{\alpha}. \tag{6}$$

The index α depends on a variety of factors such as type of active species in the CO oxidation, the surface morphology [21], etc.

Unlike pure SnO_2-based sensor (i.e. SnO_2-300), the ultradispersive SnO_2/Pd-based sensors displayed a strong influence of humidity on CO sensitivity. Fig. 8 shows a plot of relative sensor signal change ($\Delta S/S$) for 100 ppm CO at 100 °C when passing from less to more humid carrier gas, determined as

$$\Delta S/S = \frac{S(\text{r.h.1}) - S(\text{r.h.2})}{S(\text{r.h.1})}, \tag{7}$$

where r.h.1 and r.h.2 were either 5% and 15% or 15% and 30%, respectively. The rise of humidity substantially promotes the CO sensitivity of the SnO_2/Pd sensors, though this effect is more pronounced when shifting from 5% r.h. to 15% r.h. The further humidity rise from 15% to 30% leads to a slight CO response decrease, which must be due to the competitive adsorption of water occupying surface active centers and hindering CO oxidation.

Moreover, the evaluation of humidity-promoted CO response increase as a function of temperature (Fig. 9) revealed that the maximum humidity effect occurs at the temperature of 100–150 °C. This is close to the temperature of CO sensitivity maximum for the SnO_2/Pd sensors. This is an unambiguous evidence that water vapor participates in the CO oxidation during response formation. This participation can be of various kinds: formation of water derivatives (hydroxyls, associates, etc.) on the

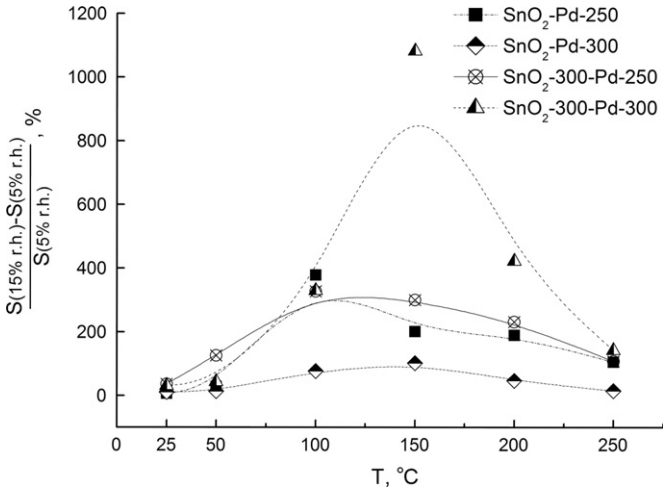

Fig. 9. Relative CO response increase for the ultradispersive SnO_2/Pd induced by relative humidity rise as a function of temperature when passing from 5% to 15% r.h.

materials surface [6,21,23], direct CO oxidation by the adsorbed H_2O molecules [20,30], labialization of the surface active centers, etc.

3.3. Analysis of processes responsible for sensor signal formation

3.3.1. XPS study under CO exposure

Upon exposing the SnO_2/Pd samples to 100 ppm CO in air (20% r.h.) at 25 °C *ex situ*, the XPS spectrum of the Pd 3*d* region changed significantly (Fig. 10) compared to that taken after pure air exposure (20% r.h.) shown in Fig. 2. The doublet with Pd $3d_{5/2}$ peak at 335.9 eV corresponding to the Pd^0 state became more prominent and its intensity was almost leveled with that of the Pd^{2+} state. Thus the Pd^0/Pd^{2+} concentration ratio increased, indicating partial PdO reduction to Pd under as small a concentration of CO in air as 100 ppm at RT. This effect was found to be reversible: after 2 hours of exposing samples to pure air the XPS spectrum of the Pd 3*d* band returned to the initial state (Fig. 2).

3.3.2. Impedance spectroscopy under variable atmosphere

The impedance spectra of SnO_2 and SnO_2/Pd powders under room conditions (air 20% r.h., $T=25$ °C) are compared in Fig. 11. The hodographs represent a high-frequency semicircle ascribed to the equivalent circuit shown in the inset of Fig. 11 and a low-frequency inclined line attributed to the contribution of proton diffusion [31–33]. The equivalent circuit includes serial resistance (R_c) attributed to electrode–powder contacts and a circuit of parallel resistance (R_v) and capacitance (C_v) corresponding to that of grains volume [31]. No contribution of grain boundaries resistance and capacitance originating from intergrain barriers were observed in the impedance spectra, which seems to be an indication of the wholly depleted grains case, when the crystallite radius is less than Debay length, which is reported to be of 3–20 nm at 25–400 °C [31]. The assignment of the observed semicircle to wholly depleted grains volume is further confirmed by low capacitance (C_v) values, calculated from the hodographs (Table 3). As can be seen C_v values are in the range 4.3–7.4 pF for different samples, which is of the same order of magnitude with the predicted capacitance for the pellets of this geometry (1.1–1.4 pF for different pellets) under an assumption of bulk SnO_2 capacitor [6]. The latter assumption considers non-porous bulk tin dioxide with dielectric constant $\varepsilon=10$ [6]. Thus the obtained experimental C_v values can be ascribed to geometrical

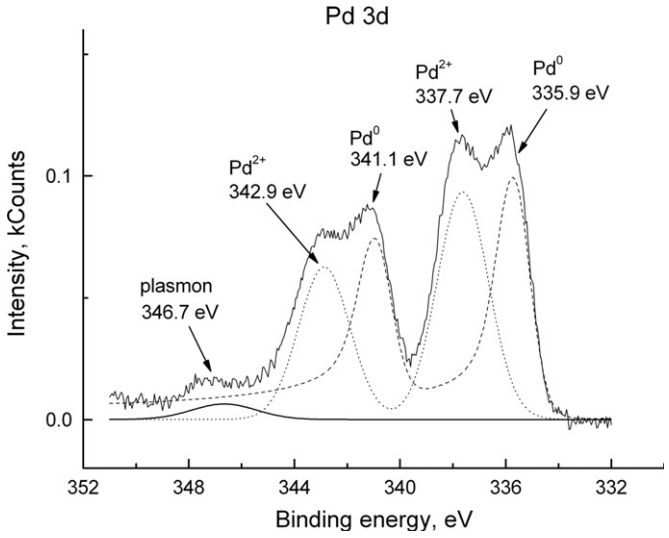

Fig. 10. XPS spectrum of the Pd 3*d* region for nanocrystalline SnO_2/Pd samples exposed to 100 ppm CO in air, $T=25$ °C, 20% r.h. Pass energy 80 eV.

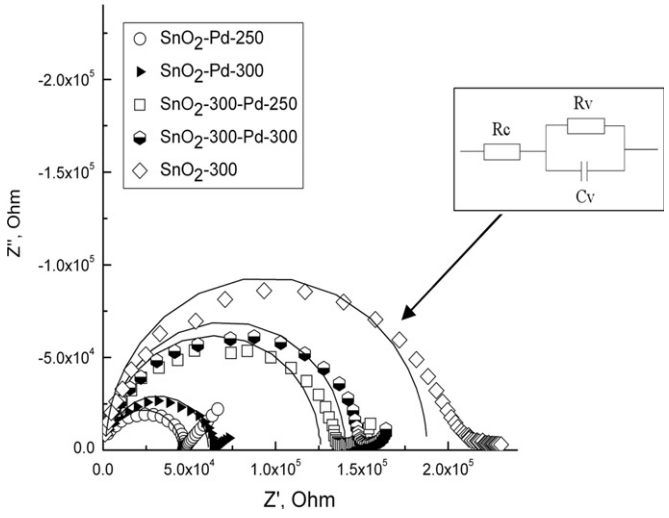

Fig. 11. Impedance spectra of ultradispersive SnO_2 and SnO_2/Pd powders under room conditions (air, 20% r.h., 25 °C).

capacitance of the tested pellets, i.e. capacitors consisting of two gold electrodes with tin dioxide interlayer. That C_v values exceed the predicted capacitance can be attributed to porous structure of pellets and/or nanoparticles agglomerates effect. Both effects lead to the pellets containing a number of internal insulating layers, increasing the whole capacitance [6].

The tested powders exhibit both electronic (σ_e) and protonic (σ_p) types of conductance when measured in the A.C. mode. To distinguish between them, we applied the Hebb–Wagner polarization method using proton blocking Au-electrodes [34,35]. The electronic conductance was defined from a stationary resistance value measured in the D.C. mode, when protons do not participate in charge transport. The protonic conductance was obtained by subtracting the D.C. electronic conductance from the reciprocal of the whole impedance, measured in the A.C. mode, when proton diffusion contributes to reversible charge transfer through the pellets:

$$\sigma_p = \sigma_\Sigma - \sigma_e = \frac{1}{Z'} - \frac{1}{R_{DC}}. \quad (8)$$

Table 3
Electrophysical parameters[a] of ultradispersive SnO_2 and SnO_2/Pd powders under variable atmosphere defined from impedance data, $T=25$ °C.

Sample	Atmosphere	R_v (kΩ)	C_v (pF)	$\sigma_\Sigma \times 10^6$ (Ω^{-1} cm^{-1})	$\sigma_e \times 10^6$ (Ω^{-1} cm^{-1})	$\sigma_p \times 10^6$ (Ohm^{-1} cm^{-1})
SnO_2-300–Pd-300	Air, 20% r.h.	100	6.0	8.50	0.90	7.60
	Air, 5% r.h.	2750	4.4	0.30	0.15	0.15
	CO/air, 5% r.h.	610	7.0	1.30	0.28	1.10
SnO_2-300–Pd-300	Air, 20% r.h.	90	6.1	9.50	0.90	8.60
	Air, 5% r.h.	3000	4.6	0.27	0.14	0.13
	CO/air, 5% r.h.	680	6.5	1.20	0.33	0.87
SnO_2–Pd-300	Air, 20% r.h.	50	6.0	18.2	1.20	17.0
	Air, 5% r.h.	1750	4.3	0.49	0.36	0.13
	CO/air, 5% r.h.	910	4.9	0.95	0.43	0.52
SnO_2–Pd-250	Air, 20% r.h.	60	6.8	13.1	1.10	12.0
	Air, 5% r.h.	1550	4.9	0.51	0.17	0.34
	CO/air, 5% r.h.	1140	5.0	0.70	0.23	0.46
SnO_2-300	Air, 20% r.h.	180	6.9	2.30	1.80	0.55
	Air, 5% r.h.	340	7.2	1.20	1.20	0.06
	CO/air, 5% r.h.	270	7.4	1.60	1.50	0.13

[a] Designations: R_v – grain volume D.C. resistance, C_v – grain volume A.C. capacitance, σ_Σ – total A.C. conductance, σ_e – electronic conductance, σ_p – protonic conductance.

The results of σ_p calculation as well as other parameters such as total conductance, grain volume resistance and capacitance defined from impedance measurements are compared in Table 3. The fit errors did not exceed 5% limit of the calculated values.

From the σ_p calculation under room conditions it follows that modifying of nanocrystalline SnO_2 by PdO/Pd gives rise to the increase of proton conductance irrespective of the SnO_2/Pd powders treatment procedure. Since the proton source in such materials was reported to be adsorbed aqueous species [31], the impedance data on the concentration of hydrated surface species is not in accordance with the TPR results related to the overall surface species concentration. We assume that in hydrogen consumption during TPR the contribution of adsorbed water derivatives (hydroxyls) is less than that of the chemisorbed oxygen species, O_2^- or O^-. In any case, the promotive effect of PdO/Pd deposition on the SnO_2 surface aqueous species concentration is a noteworthy feature and may be one of the factors affecting the SnO_2/Pd sensitivity to CO at room temperature.

The relative humidity decrease from 20% to 5% at RT resulted in both electronic and protonic conductance diminishing (Table 3). The corresponding impedance spectra change are depicted in Fig. 12 (transition *a*–*b*). The decrease of both electronic and protonic conductance is explained by adsorbed water molecules that exhibit both electron and proton donor properties due to the presence of both free electron pairs and acidic protons [6].

When 100 ppm CO is added to air at fixed humidity (5% r.h.), at RT the impedance spectra change as shown in Fig. 12 (transition *b*–*c*). The electrophysical parameters calculated from the corresponding hodographs are compared in Table 3. In addition to the expected electronic conductance rise, the CO exposure also led to the protonic conductance increase. Furthermore, the trend of absolute protonic conductance increase among the tested samples correlates with the sensor responses to 100 ppm CO at RT (Fig. 13), so that the most sensitive SnO_2-300–Pd-300 sample exhibits the highest protonic conductance increase. This suggests that CO oxidation on the surface of the sensitive material at RT is accompanied by H^+ emission; therefore the hydrogen atoms participate in the reaction with CO. The source of hydrogen atoms must be surface species on the sensitive material, e.g. surface hydroxyls or other hydrogen containing species. The latter seem to be reactive enough to oxidize CO even at room temperature, giving rise to sensor response and yielding H^+ (or hydrated proton species) as a product. The correlation between σ_p and S_{CO} is violated by the SnO_2–Pd-250 sample, which might be due to its highest background protonic conductance compared with other powders, so that σ_p enhancement could be not so pronounced.

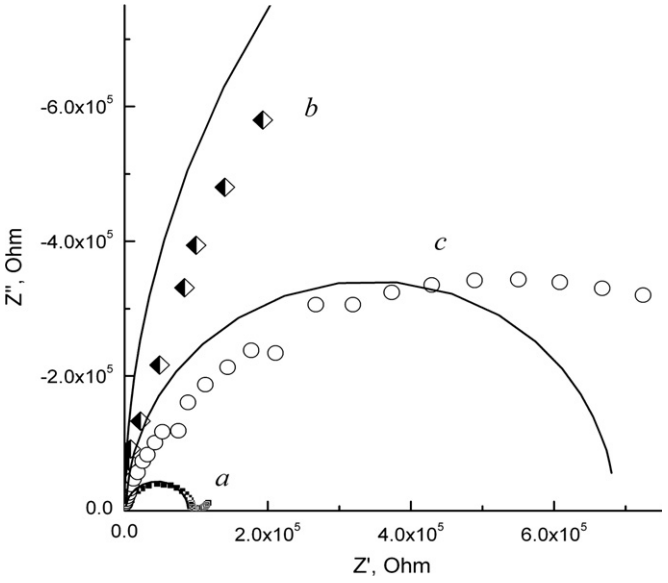

Fig. 12. Typical impedance spectra of ultradispersive SnO_2 and SnO_2/Pd samples in air at 20% r.h. (a), air at 5% r.h. (b), 100 ppm CO in air at 5% r.h. (c), $T=25$ °C.

Hence, the effect of tin dioxide modifying by PdO/Pd and of the SnO_2/Pd treatment on the CO sensitivity seems to be not only in the CO oxidation by PdO (as indicated by the XPS measurements), but also in the promotion of direct CO reaction with the surface hydrated species. Yet, the actual influence of PdO/Pd on the concentration and reactivity of the surface aqueous species remains unclear. We can only assume that PdO results in some electronic effect, e.g. the PdO/Pd clusters accept electrons from the SnO_2 grains and the latter tend to accumulate donor-like molecules, such as H_2O, on the grain boundaries.

3.3.3. FTIR analysis under variable relative humidity

FTIR investigation of the ultradispersive SnO_2 and SnO_2/Pd powders under the air atmosphere at 20% r.h. and 5% r.h. at RT was performed to evaluate the initial surface species composition, find out which of them could be reactants in the room

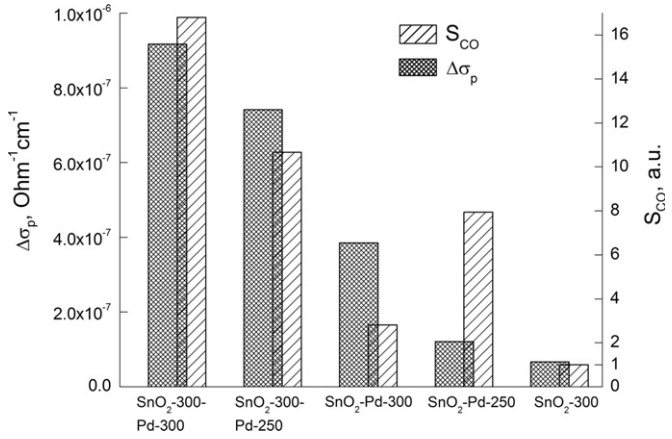

Fig. 13. Comparison of absolute σ_p growth for different samples upon CO exposure with CO sensor signal.

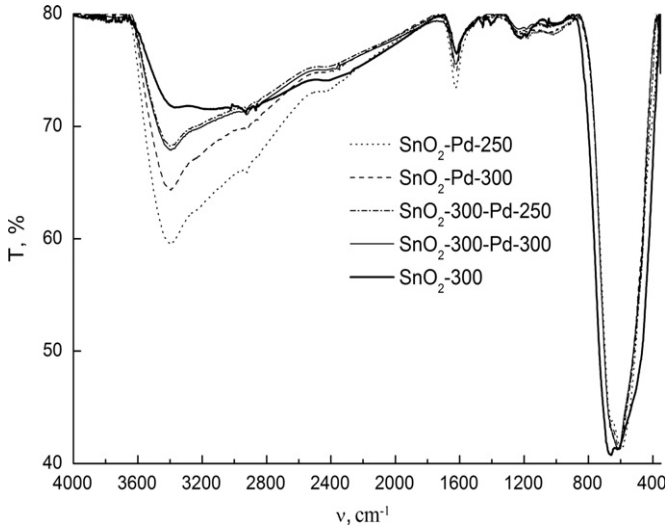

Fig. 14. FTIR spectra of ultradispersive SnO_2 and SnO_2/Pd samples under air 20% r.h., T=25 °C.

temperature CO oxidation (as discussed in the previous paragraph) and study the effect of PdO/Pd deposition on the surface species composition. Fig. 14 shows the spectra of powders under air at 20% r.h. To evaluate the relative concentration of chemisorbed surface species with respect to an amount of lattice O–Sn–O bonds, we subtracted baseline and normalized the spectra to IR absorbance at 670 cm^{-1} corresponding to O–Sn–O stretching mode [36]. The 800–400 cm^{-1} band corresponds to the metal–O vibrations; in addition, the peak at 670 cm^{-1} compiles peaks at 590 and 470 cm^{-1}, which may be attributed to terminal Sn–OH bonds and to SnO_2 bulk phonons, respectively [36]. Fig. 14 indicates that the powders contain mostly aqueous surface species with a wide absorption band at 3500–900 cm^{-1}. The maximum of the band at about 3400 cm^{-1} is an evidence for predominant rooted hydroxyls associated via hydrogen bonds (OH…OH) [19]. The data indicate that the introduction of PdO/Pd into the ultradispersive SnO_2 results in surface species concentration increase, the rise being most significant at 3400 cm^{-1}. Moreover, the sequence of surface hydroxyls concentration rise through the tested samples is the same as that of the proton conductance increase evaluated from the impedance data (see Table 3). Agreement between FTIR and impedance data allows us to conclude that the deposition of PdO/Pd on the tin dioxide surface is accompanied by the rise of surface hydroxyl groups concentration (especially in the form of the OH…OH associates).

The decrease of humidity down to 5% r.h. yielded a common decrease of the aqueous surface species, the overall amount of those through the samples being leveled (Fig. 15). However, detailed study (Fig. 15 inset) revealed that the sample SnO_2-300–Pd-300, which showed the highest sensor response to CO at RT, displayed the most prominent peak at 3400 cm^{-1}. From FTIR data for the surface species composition and its comparison with low-temperature CO sensing behavior we deduced that the species that could oxidize CO at low (room) temperature (and thus form the sensor signal) are OH…OH associates. Besides, this type of tin dioxide surface hydroxyls was shown to react [19] with CO at 200 °C.

3.3.4. *Notes on the processes of SnO_2/Pd materials interaction with CO during sensor signal formation*

On the basis of the reported study we suggest the following qualitative model as an attempt to describe the complex effect of nanocrystalline tin dioxide sensibilization by Pd additive towards CO sensing at temperatures as low as RT.

(a) It is known that the CO detection by SnO_2-based sensors occurs via surface oxidation processes by chemisorbed oxygen species [16]:

$$CO_{(g)} + O^-_{(surf)} = CO_{2(g)} + e^-_{(bulk)}, \quad (9)$$

$$2CO_{(g)} + O^-_{2(surf)} = 2CO_{2(g)} + e^-_{(bulk)}. \quad (10)$$

Yet, these reactions can proceed at elevated temperatures only [17]. In the sensing test on the pure SnO_2-based sensors we noted that the minimal temperature for the initiation of such processes is 150 °C for the ultradispersive SnO_2-300 sample and 200–250 °C for the rougher SnO_2-500 sample. We suppose that these reactions proceed on the SnO_2/Pd surface also on the areas free from the PdO/Pd clusters, i.e. on the active sites analogous to that of pure SnO_2.

(b) The strong sensibilization effect of PdO/Pd clusters that leads to room temperature CO sensitivity and the downwards shift of applicable operating temperature must be due to the formation of new active sites, which are more reactive towards CO at low (room) temperature than the chemisorbed oxygen species. The XPS study of the room temperature–CO

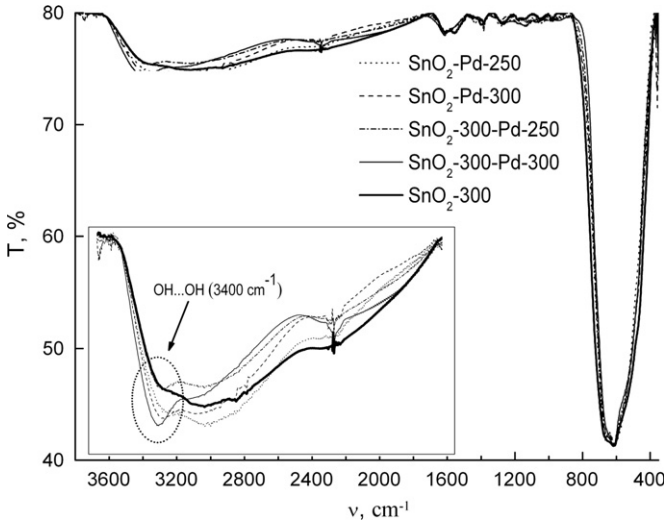

Fig. 15. IR spectra in the 3800–900 cm^{-1} region for ultradispersive SnO_2 and SnO_2/Pd samples under air 5% r.h., T=25 °C. Inset: enlarged spectra in 3700–1700 cm^{-1} region.

interaction with the SnO_2/Pd powders showed that these new active sites include the PdO/Pd clusters:

$$CO_{(g)} + PdO_{(s)} = CO_{2(g)} + Pd_{(s)}. \quad (11)$$

The role of PdO/Pd might be an initiation of CO oxidation at room temperature via a reaction similar to (11). The initiating function is attributed to process (11), since it was the only process determining the sensor response, the difference in CO sensitivity between the samples would be due to the difference in the Pd concentration. In contrast, the Pd concentration for different samples was found to be similar, while the CO sensitivity was obviously different. Besides, the reduction of PdO must have removed the Schottky barriers between PdO and SnO_2 yielding the increase of the sensors conductance, as the former is a *p*-type semiconductor with work function (WF)$\sim$6 eV and the latter is an *n*-type semiconductor (WF=4.7 eV), while for metallic Pd the work function (4.8 eV) is close to that of SnO_2 [14].

(c) The role of SnO_2/Pd surface hydroxyls in the interaction with CO cannot be overrated. The direct CO oxidation by OH-groups (rooted OH…OH associates, according to the FTIR data) via a process like (12) is a suitable explanation for both the impedance data (protonic conductance increase upon CO exposure) and the promotive humidity effect on CO sensitivity:

$$CO_{(g)} + OH_{(surf)} = CO_{2(g)} + H^+_{(surf)} + e^-_{(bulk)}. \quad (12)$$

The appearance of a maximum on the response–temperature dependence in the low-temperature range (near 100 °C) is likely due to hydroxyls recombination and desorption at heating up to temperatures exceeding 100 °C. On the other hand, when the temperature is below 100 °C a competitive molecular water adsorption seems to occur that shields active surface sites. The effect of the OH-groups is more pronounced for SnO_2/Pd rather than for SnO_2 samples, which might be due to the promotive effect of PdO/Pd on the hydroxyls concentration (evidenced in FTIR experiment), an initiating role of PdO in the process (11) or catalytic properties of the PdO/Pd clusters.

(d) The enhanced reactivity of OH-groups at low (room) temperature compared with the chemisorbed oxygen species could result from a chain character of the process (12): the liberated H^+ ions (or hydrated proton species) may regenerate the rooted hydroxyls via combination with bridging oxygen ions from the SnO_2 lattice:

$$H^+_{(surf)} + O^{2-}_{(lat)} = OH_{(surf)} + e^-_{(bulk)}. \quad (13)$$

Besides recovering surface species that are able to oxidize CO at room temperature, this should lead to additional conductance increase, since the formed hydroxyls were reported to be electron donors [21].

4. Conclusions

Nanocrystalline SnO_2/Pd composites for room temperature CO gas sensing applications were synthesized via an aqueous precipitation route followed by impregnation of $Pd(acac)_2$ and thermal treatment. Based on the XRD, TEM, BET and XPS data, the system was taken to comprise of SnO_2 nanocrystals with the PdO/Pd clusters attached to the SnO_2 surface. The study of the effect of sample treatment indicated that higher CO sensitivity was displayed by nanocomposites obtained via the PdO/Pd deposition on the surface of crystallized SnO_2 powder rather than amorphous hydrated $SnO_2 \cdot nH_2O$ powder. Investigation of the CO interaction with the gas sensitive materials at room temperature revealed PdO reduction as well as reaction with OH-groups yielding protons or hydrated proton species. Finally, the qualitative model of complex SnO_2/Pd – CO interaction responsible for low (room) temperature CO sensitivity of the nanocomposites was suggested. The model includes CO oxidation by the PdO/Pd clusters at low temperature as an initiating step in the chain of CO reactions involving the surface OH-groups.

Acknowledgments

This work was supported by FP7-NMP-2009 EU-RU project 247768 S3 and Russian Agency “Rosnauka” project 02.527.11.0008. The authors thank Dr. A.P. Bobylev and Dr. R.B. Vasiliev for their assistance and discussion. The authors thank Dr. V. Neudachina for remarks and corrections.

Appendix A. Supplementary material

Supplementary data associated with this article can be found in the online version at doi:10.1016/j.jssc.2010.07.017.

References

[1] M. Batzill, U. Diebold, Prog. Surf. Sci. 79 (2000) 47.
[2] G. Korotcenkov, S.-D. Han, B.K. Cho, V. Brinzari, Critical Reviews in Solid State and Materials Sciences 34 (2009) 1.
[3] N. Yamazoe, Sens. Actuators B 108 (2005) 2.
[4] M.-I. Baraton, L. Merhari, H. Ferkel, J.-F. Castagnet, Mater. Sci. Eng. C 19 (2002) 315.
[5] M.-I. Baraton, Proceedings of the NATO Advanced Study Institute on Sensors for Environment, Health and Security: Advanced Materials and Technologies Vichy (France), 16–27 September 2007, p. 31.
[6] J. McAleer, P. Moseley, J. Norris, D. Williams, J. Chem. Soc. Faraday Trans. 83 (1987) 1323.
[7] S. Wang, Y. Zhao, J. Huang, Y. Wang, H. Ren, S. Wu, S. Zhang, W. Huang, Appl. Surf. Sci. 253 (2007) 3057.
[8] B. Bahrami, A. Khodadadi, M. Kazemeini, Y. Mortazavi, Sens. Actuators B 133 (2008) 352.
[9] J.T. McCue, J.Y. Ying, Chem. Mater. 19 (2007) 1009.
[10] N. Yamazoe, Y. Kurokawa, T. Seiyama, Sens. Actuators 4 (1983) 283.
[11] N.S. Ramgir, Y.K. Hwang, S.H. Jhung, I.S. Mulla, J.-S. Chang, Sens. Actuators B 114 (2006) 275.
[12] Y.-S. Lee, O.-S. Kwon, S.-M. Lee, K.-D. Song, C.-H. Shim, G.-H. Rue, D.-D. Lee, Sens. Actuators B 93 (2003) 556.
[13] V.V. Malyshev, A.V. Pislyakov, Sens. Actuators B 123 (2007) 71.
[14] O.V. Safonova, M.N. Rumyantseva, L.I. Ryabova, M. Labeau, G. Delabouglise, A.M. Gaskov, Mater. Sci. Eng. B 85 (2001) 43.
[15] J. Kim, S.D. Han, I. Singh, H.D. Lee, J.S. Wang, Sens. Actuators B 107 (2005) 825.
[16] M. Epifani, J. Arbiol, E. Pellicer, E. Comini, P. Siciliano, G. Faglia, J.R. Morante, Cryst. Growth Design 8 (5) (2008) 1774.
[17] R. Rella, P. Siciliano, S. Capone, M. Epifani, L. Vasanelli, A. Licciulli, Sens. Actuators B 58 (1999) 283.
[18] J.C. Belmonte, J. Manzano, J. Arbiol, A. Cirera, J. Puigcorbe, A. Vila, N. Sabate, I. Gracia, C. Cane, J.R. Morante, Sens. Actuators B 114 (2006) 881.
[19] D. Koziej, N. Barsan, K. Shimanoe, N. Yamazoe, J. Szuber, U. Weimar, Sens. Actuators B 118 (2006) 98.
[20] N.N. Samotaev, A.A. Vasiliev, B.I. Podlepetsky, A.V. Sokolov, A.V. Pisliakov, Sens. Actuators B 127 (2007) 242.
[21] N. Barsan, U. Weimar, J. Phys. Condens. Matter 15 (2003) 813.
[22] S. Harbeck, A. Szatvanyi, N. Barsan, U. Weimar, V. Hoffmann, Thin Solid Films 436 (2003) 76.
[23] V.A. Gercher, D.F. Cox, Surf. Sci. 322 (1-3) (1995) 177.
[24] A.S. Ivanova, E.M. Slavinskaya, R.V. Gulyaev, V.I. Zaikovskii, O.A. Stonkus, .G. Danilova, L.M. Plyasova, I.A. Polukhina, A.I. Boronin, Appl. Catal. B: Environ. 97 (2010) 57.
[25] D. Chichova, P. Maki-Arvela, T. Heikkila, N. Kumar, J. Vayrynen, T. Salmi, D.Yu. Murzin, Top Catal. 52 (2009) 359.
[26] T. Wu, W.E. Kaden, W.A. Kunkel, S.L. Anderson, Surf. Sci. 603 (2009) 2764.
[27] K. Veltruska, N. Tsud, V. Brinzari, G. Korotchenkov, V. Matolin, Vacuum 61 (2001) 129.
[28] N.V. Kramareva, A.Yu. Stakheev, O.P. Tkachenko, K.V. Klementiev, W. Grünert, E.D. Finashina, L.M. Kustov, J. Molec. Catal. A: Chem. 209 (2004) 97.
[29] E.V. Golubina, E.S. Lokteva, V.V. Lunin, N.S. Telegina, A.Yu. Stakheev, P. Tundo, Appl. Catal. A: General 302 (2006) 32.

[30] A. Ahmad, J. Walsh, T.A. Wheat, Sens. Actuators B 93 (2003) 538.
[31] R.B. Vasiliev, M.N. Rumyantseva, S.G. Dorofeev, Y.M. Potashnikova, L.I. Ryabova, A.M. Gaskov, Mendeleev Commun. (2004) 167.
[32] Yu. Dobrovolsky, L. Leonova, S. Nadkhina, N. Panina, Solid State Ionics 119 (1999) 275.
[33] S. Hara, S. Takano, M. Miyayama, J. Phys. Chem. B 108 (2004) 5634.
[34] C. Gabrielli, P.P. Grand, A. Lasia, H. Perrota, J. Electrochem. Soc. 151 (11) (2004) A1925.
[35] S. Hara, M. Miyayama, Solid State Ionics 168 (2004) 111–116.
[36] Y. Liu, F. Yang, X. Yang, Colloid Surf. A: Physicochem. Eng. Aspects 312 (2008) 219.